ACS APPLIED MATERIALS & INTERFACES

www.acsami.org

Research Article

Linear versus Nonlinear Aromatic Polyamides: The Role of Backbone Geometry in Thin Film Salt Exclusion Membranes

Anna C. Fraser, Nick Guan Pin Chew, Maruti Hegde, Fei Liu, Chih-Wei Liu, Orlando Coronell,* and Theo J. Dingemans*

Cite This: *ACS Appl. Mater. Interfaces* 2022, 14, 36143−36156

Read Online

ACCESS | Metrics & More | Article Recommendations | Supporting Information

ABSTRACT: Two aromatic polyamides—poly(3,3′-dihydroxybenzidine terephthalamide) (DHTA) and poly(3,3′-dihydroxybenzidine isophthalamide) (DHIA)—are compared for their ability to remove salts from water. DHTA is linear and rigid whereas DHIA is nonlinear and semirigid. DHTA and DHIA were selected as they allow us to investigate the effect of polymer backbone geometry on salt exclusion in a non-crosslinked thin film membrane, independently of the backbone chemistry. Because of their differences in solution viscosity, spin coating parameters for DHTA and DHIA solutions were optimized separately to produce thin film composites (TFCs) with reproducible membrane properties. The resulting DHTA TFCs displayed salt rejections of 87.8% (NaCl), 97.0% ($MgSO_4$), and 80.3% ($CaCl_2$). In comparison, DHIA TFCs demonstrated poor salt rejections of 21.0% (NaCl), 29.3% ($MgSO_4$), and 15.4% ($CaCl_2$). Cross-sectional SEM images of DHTA and DHIA films reveal that DHTA has a stratified (layered) morphology whereas DHIA exhibits a dense, featureless morphology. Both DHTA and DHIA TFCs exhibit similar surface morphology, contact angle, surface charge, and water uptake. PEG rejection experiments indicate that the average pore size of DHTA TFCs is ∼2 nm while DHIA TFCs have an average pore size of ∼3 nm. Our findings illustrate that using a rigid, linear aromatic polyamide gives an active layer with a stratified morphology, uniplanar orientation, smaller pores, and higher salt rejection, whereas the nonlinear aromatic polyamide analogue results in an isotropic active layer with larger pores and lower salt rejection.

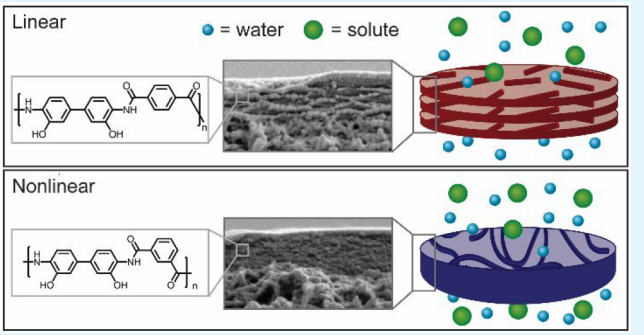

KEYWORDS: *nanofiltration, membrane processing, polymer backbone geometry, linear versus nonlinear aromatic polyamide, membrane morphology*

1. INTRODUCTION

Polymeric membrane technologies offer cost-effective and energy-efficient means of removing unwanted species from water.[1−5] Two types of pressure-driven membranes, reverse osmosis (RO) and nanofiltration (NF), remove salts and small molecules from water sources by using membrane pore sizes within the approximate ranges of 0.1−1 nm (RO) and 1−2 nm (NF).[6,7] The active layer in current state-of-the-art RO and NF membranes is based on aromatic polyamides formed via the interfacial polymerization of a diamine and an acid chloride (active layer thickness ∼10−200 nm). This interfacial polymerization is performed on top of a microporous polysulfone support to yield a thin film composite (TFC).[5−11] The active layers for RO and NF membranes are predominantly fabricated by using *m*-phenylenediamine (MPD) and trimesoyl chloride (TMC), forming a nonlinear covalently crosslinked and branched polyamide structure (MPD-TMC), as shown in Figure 1.[5,7] The performance of an active layer as an RO or NF membrane is dictated by multiple, interdependent properties such as pore size, free volume, and crosslink density.[5,7] These properties can be tuned by varying interfacial polymerization conditions, that is, monomer concentration, polymerization time, and so on, as well as thermal and solvent post-treatment protocols.[12−17] A commonly studied NF active layer is produced by introducing piperazine (PIP) as a comonomer to MPD or by altogether replacing MPD with PIP and reacting with TMC, forming poly(piperazine-amide) (PIP-TMC) (Figure 1).[6,7,18]

Despite the prominent use of these polymers for RO and NF applications, our understanding of how polymer backbone geometry affects polymer processing, thin film properties, and transport and rejection of molecular and ionic species within the active layer remains limited.[19,20] Fabricating membranes

Received: June 1, 2022
Accepted: July 25, 2022
Published: July 28, 2022

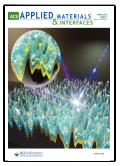

https://doi.org/10.1021/acsami.2c09810
ACS Appl. Mater. Interfaces 2022, 14, 36143−36156

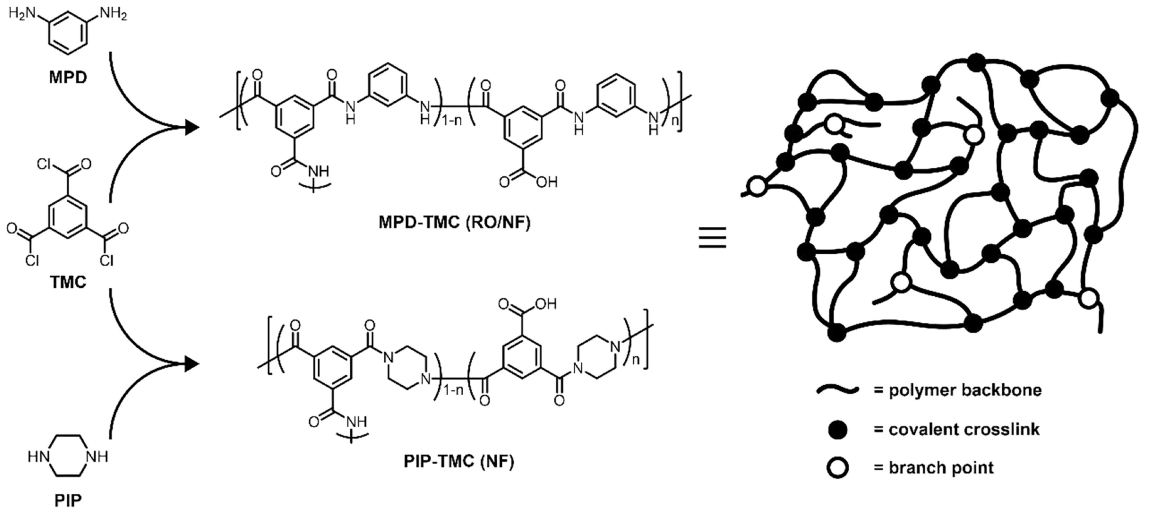

Figure 1. Synthesis and chemical structures of commonly used RO and NF active layers formed by MPD-TMC and PIP-TMC. The use of TMC, a trifunctional monomer, results in a crosslinked polyamide network. An illustration of the resulting crosslinked polyamide network is also shown.

via interfacial polymerization produces an active layer with a range of densities (~0.9−1.2 g cm^{-3}) and pore sizes (~0.2−0.5 nm, RO, or 0.7−1.2 nm, NF).[21−24] The stochastic nature of the interfacial polymerization process and the inhomogeneities (e.g., density and pore size distribution) of the active layer complicate efforts to establish fundamental structure−property relationships. The low thickness of the active layer (10−200 nm) and the insolubility arising from covalently crosslinked networks make characterization of the interfacial layer post-fabrication difficult. Though advances in electron microscopy imaging techniques have enabled better understanding of the overall membrane structure—such as characterizing void volume fraction (0.04−30%), density variations across the polyamide layer, and the effect of the polysulfone substrate on morphology—researchers have yet to visualize the exact polymer structure of the interfacial layer at a molecular level.[21,22,25−30] This gap in fundamental knowledge regarding structure−property relationships precludes membrane scientists from rationally designing next-generation membrane technologies.

We propose using two simple aromatic polyamide model polymers to gain insights into the role of polymer geometry on RO and NF membrane processing, structure, and performance: an aromatic linear, rigid, rodlike polyamide versus an aromatic nonlinear polyamide. The linear polyamide—poly(3,3′-dihydroxybenzidine terephthalamide) (DHTA)—has a rodlike structure due to the 180° exocyclic bond angle introduced by the *para*-substituted acid chloride (terephthaloyl chloride) in the polymer backbone (Figure 2).[31] The high persistence length of rodlike DHTA enables it to form nematic, lyotropic solutions in alkaline solutions.[31] By contrast, the nonlinear polyamide—poly(3,3′-dihydroxybenzidine isophthalamide) (DHIA) (Figure 2)—prepared by using a *meta*-substituted acid chloride (isophthaloyl chloride), contains a 120° exocyclic bond angle. This disrupts the linearity of the polymer backbone, resulting in a nonlinear or kinked structure.[32,33] Note here that the term linear applies to the polymer DHTA, synthesized from only difunctional *para*-substituted monomers, whereas nonlinear is used to describe DHIA, which is synthesized from a difunctional *para*- and *meta*-substituted monomer. Neither polymer is crosslinked.

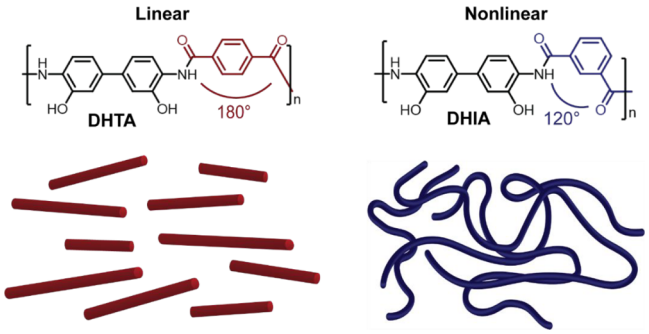

Figure 2. Molecular structure of poly(3,3′-dihydroxybenzidine terephthalamide) (DHTA) which possesses an exocyclic bond angle of 180°, resulting in a rodlike linear structure. Contrastingly, an exocyclic bond angle of 120° makes poly(3,3′-dihydroxybenzidine isophthalamide) (DHIA) kinked and nonlinear.

Herein, we demonstrate how DHTA and DHIA solutions can be spin coated onto microporous polysulfone−polypropylene (PSf) supports to form a TFC with a non-crosslinked active layer. Using chemically identical DHTA and DHIA enables us to study how polymer backbone geometry affects the processing, morphology of polymer membranes and their resulting membrane performance. Moreover, this work expands upon the use of linear, rodlike polyamides as desalting membranes.[34−37] The fundamental knowledge imparted by this work shows the importance of polymer geometry in designing polymers for desalting membranes.

2. RESULTS AND DISCUSSION

2.1. Polymer Characterization. DHTA and DHIA obtained by solution polymerization were characterized by using several techniques. Fourier transform infrared spectroscopy (FTIR) provided evidence of amide functionalities (Figure S1, Supporting Information). The peaks at 1643 and 1647 cm^{-1} (DHTA and DHIA, respectively) are attributed to amide I. We believe peaks at ~1525 and ~1512 cm^{-1} (DHTA and DHIA, respectively) correspond to amide II absorbances.[38] The broad peaks between ~2900 and ~3500 cm^{-1} (DHTA and DHIA, respectively) arise from the presence of

https://doi.org/10.1021/acsami.2c09810
ACS Appl. Mater. Interfaces 2022, 14, 36143−36156

Scheme 1. Deprotonation and Reprotonation of DHTA and DHIA Using a Strong Base (NaOH) and Strong Acid (Hydrochloric Acid, HCl)

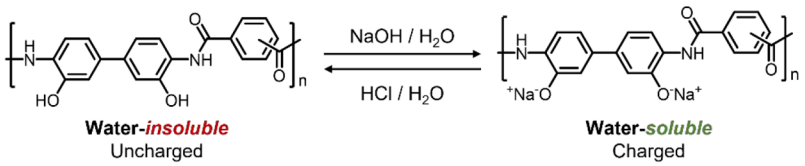

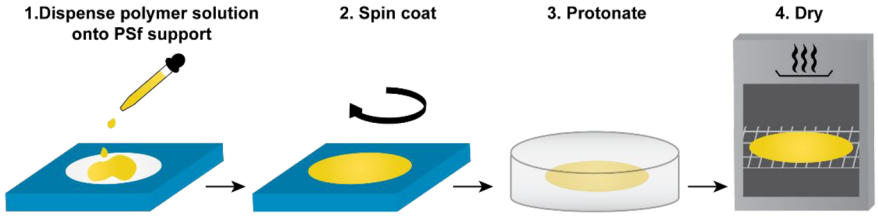

Figure 3. Fabrication of DHTA and DHIA TFC membranes. (1) DHTA (2 wt %) or DHIA (4 wt %) solution was dispensed onto a 6.75 cm diameter PSf coupon, fully coating the substrate, and allowed to soak into the PSf coupon for 6 min. (2) The TFC was spin coated for 1 min to form an active layer (1000 or 3000 rpm). (3) The active layer was protonated in HCl (DHTA: 1 or 0.001 M; DHIA: 1 M), soaked in LGW (10 min), and then placed in HCl again for 2 min. (4) After a final rinse in LGW (3 min) the DHTA or DHIA TFC was dried in an oven at 60 °C.

water, −OH, and H-bonded and non-H-bonded amide peaks.[39]

Nuclear magnetic resonance spectroscopy (NMR) confirmed the structure of DHTA and DHIA (Figure S2). While DHIA dissolved quickly in deuterated dimethyl sulfoxide (DMSO-d_6) for NMR, DHTA exhibited limited solubility in common organic solvents such as DMSO due to the rigidity of its backbone. Instead, DHTA was dissolved in a 20:1 v/v mixture of DMSO-d_6 and a 40 wt % solution of sodium deuteroxide (NaOD) in deuterated water (D_2O). The NaOD aided in deprotonating the hydroxyl protons, increasing DHTA's solubility in DMSO-d_6. The protons of the hydroxyl and amide bond (−OH and −NH) are absent from the DHTA ^{1}H NMR spectra (Figure S2a) because these protons rapidly exchanged with deuterium, which is ^{1}H NMR inactive, in the presence of NaOD and D_2O.[40] The presence of NaOD causes the rodlike DHTA to become charged and presumably form molecular aggregates.[31] The peak broadening observed in the ^{1}H NMR spectrum (Figure S2a) of DHTA is thus attributed to the slower tumbling—long time scales—of rodlike molecular aggregates.[41] Comparatively, DHIA solutions dissolved in DMSO-d_6, without NaOD, and gave well-resolved NMR peaks (Figure S2b) as DHIA was in the uncharged state. Peak integrations of DHTA and DHIA matched the expected number of hydrogens along the polymer backbones.

The relative molecular weights of DHTA and DHIA were determined by using size exclusion chromatography (SEC) (Table S1). DHTA and DHIA were dissolved and measured in *N*-methyl-2-pyrrolidone (NMP) containing 30 mmol of lithium bromide (LiBr) and 30 mmol of phosphoric acid (H_3PO_4) as the mobile phase. The reported molecular weights were obtained by comparing with linear polystyrene calibration standards. The weight-average molecular weight (M_w) of DHTA was 212500 g mol^{-1} with a dispersity ($Đ$) of 2.5 while DHIA was 185000 g mol^{-1} with a $Đ$ of 2.1 (Table S1), with both polymers being unimodal (Figure S3). Robust and flexible bulk films could be prepared from both polymer solutions, indicating sufficiently high molecular weights were achieved.

Thermal gravimetric analysis probed the dynamic thermal stability of DHTA and DHIA as a function of temperature (Figure S4). DHTA and DHIA dehydrated and cyclized at temperatures between 200 and 450 °C to form the polybenzoxazole derivative, resulting in a weight loss of 10.8 and 10.5 wt %, respectively (Scheme S1). The experimental weight loss values closely agree with the theoretical value of 10.4 wt % for complete loss of water that accompanies the cyclization reaction. This confirms the presence of hydroxyl groups on both DHTA and DHIA.

2.2. Membrane Fabrication. DHTA and DHIA were dissolved in a basic solution (i.e., pH > 12) of sodium hydroxide (NaOH) in deionized (DI) water and spin coated onto PSf to form TFCs. Solutions of DHTA and DHIA in NaOH/DI water appeared dark brown due to formation of the phenoxide. Reprotonation of the polymers using a strong acid (i.e., pH 1) resulted in cohesive DHTA and DHIA active layers. Scheme 1 depicts the reversible process of solubilizing DHTA and DHIA and then converting back to a water-insoluble layer.

The fabrication of both DHTA and DHIA followed the general procedure outlined in Figure 3, where after spin coatingthe polymer solution, the TFC was submerged in an HCl bath, swelled in lab-grade water (LGW, resistivity ≥17.8 MΩ·cm), and then dipped briefly into HCl again before a final rinse in LGW.

Experiments with varied initial protonation time in HCl (1 or 20 min) yielded TFCs with similar membrane properties (Figure S5). Therefore, the initial protonation time was maintained at 5 min. After fabrication, the TFC was dried in an oven. Heat treatment of membranes post-fabrication has been shown to promote the densification of the polymer active layer, decreasing defects and increasing salt rejection of the membrane.[12] Nondried TFCs demonstrated zero salt rejection with high water permeance and could not withstand pressures greater than 100 psi. Therefore, heat treatment had the added benefit of improving the mechanical performance of the active layer.

While the general procedure in Figure 3 was used for both polymers, spin coating parameters for each polymer were optimized separately. DHTA solutions are more viscous than

https://doi.org/10.1021/acsami.2c09810
ACS Appl. Mater. Interfaces 2022, 14, 36143−36156

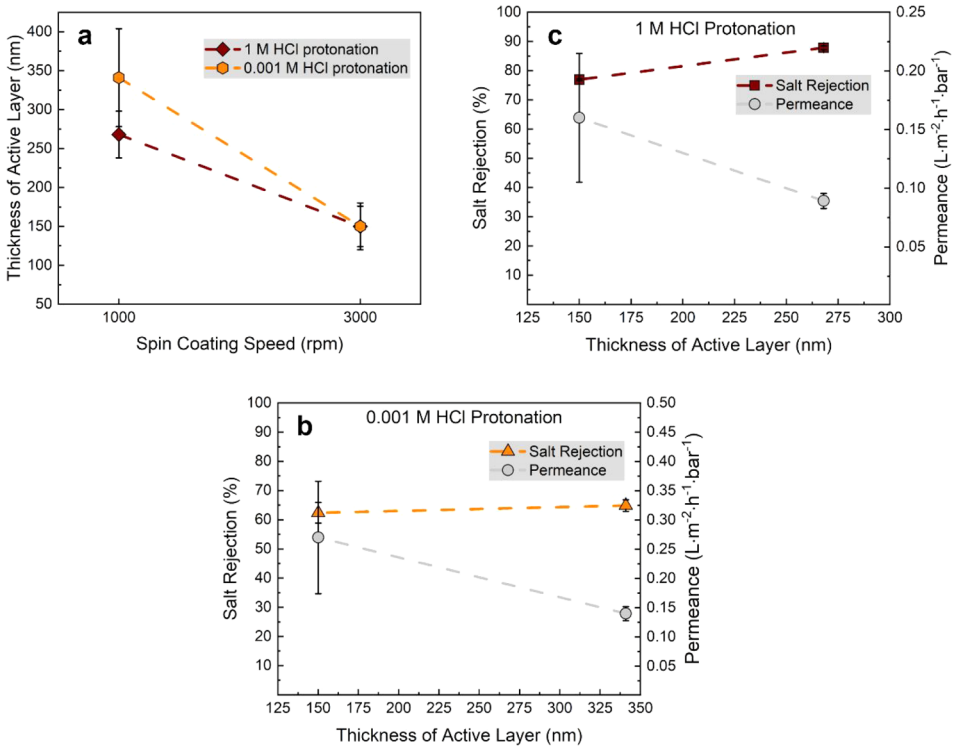

Figure 4. Properties of spin coated DHTA TFCs. (a) Correlation of active layer thickness to the spin coating speed and acid strength as found by measuring cross sections of SEM images. Salt rejection and water permeance when spin coated DHTA was protonated in (b) 1 M HCl and (c) 0.001 M HCl. All DHTA TFCs were tested with 2000 ppm of NaCl at 400 psi and pH 5.2 in dead-end mode. Dashed lines are provided as a guide to the eye.

the corresponding DHIA solutions. This difference in solution viscosity may be directly related to the backbone geometry and/or differences in absolute molecular weights.[42,43] Solution viscosity is a critical parameter for spin coating as it impacts the resulting active layer thickness, which in turn affects the membrane performance.

We evaluated the processing conditions of DHTA and DHIA TFCs by examining the membrane performance of the resulting TFC (i.e., water permeance and salt rejection of 2000 ppm of NaCl in water). The interplay of polymer geometry, polymer processing, and TFC properties is provided in sections 2.3 and 2.4.

2.3. DHTA TFC Fabrication and Performance. We used a 2 wt % DHTA solution for spin coating as higher concentrations of DHTA yielded solutions that were too viscous for spin coating. The thickness of the active layer was controlled by adjusting the spin coating speed. SEM measurements of the DHTA active layer thickness revealed that the thickness decreased as spin coating speed increased from 1000 to 3000 rpm, as expected (Figure 4a).[44]

We visually observed that the spin coated layer appeared drier after spin coating at 3000 rpm compared to 1000 rpm. For DHTA active layers spin coated at 1000 rpm, protonation with 0.001 M HCl resulted in significantly thicker membranes compared to protonation with 1 M HCl—341 and 267 nm, comparatively (Figure 4a). Spin coating at 3000 rpm, by contrast, gave active layers of the same thickness despite protonation in 0.001 or 1 M HCl. We rationalize the difference in film thicknesses as follows. The kinetics of protonation with 0.001 M HCl would be slower than with 1 M HCl, a significantly stronger acid. Protonation of the wetter (visually) 1000 rpm spin coated active layer with 0.001 M HCl allowed the layer to swell more compared to protonation with 1 M HCl. As spin coating at 3000 rpm appeared to give a drier active layer, the active layer did not swell as significantly in either 0.001 or 1 M HCl.

DHTA TFCs protonated with 1 M HCl showed decreasing salt rejection (NaCl) with decreasing active layer thickness (Figure 4b). The correlation of membrane fabrication conditions to the resulting properties is difficult to determine as salt rejection and water permeance result from the interplay of many factors. At higher spin coating speeds, thinner and drier active layers are formed that can in turn influence the phase inversion process.[45,46] The lower salt rejection and higher water permeance for active layers fabricated by using 3000 rpm suggest the presence of defects. DHTA TFCs spin coated at 1000 rpm resulted in the highest salt rejection (87.8%) with a water permeance of 0.09 L m^{-2} h^{-1} bar^{-1} (Figure 4b). Protonation using 1 M HCl produced DHTA TFCs with higher salt rejection values (76.9−87.8%) compared with 0.001 M HCl (62.3−64.8%) (Figure 4b,c). We speculate that longer coagulation time of the active layer with 0.001 M HCl compared to 1 M HCl protonation may have introduced a looser structure, which led to a larger average pore size. Our results agree with other reports on the effect of coagulation time on pore development of membranes formed via phase inversion, whereby slower coagulation provides more time for polymer-poor regions to form in the membrane, resulting in larger pores.[45,46] Because of their relatively high NaCl rejection and reproducibility, DHTA TFCs spin coated at 1000 rpm and protonated with 1 M HCl were used for the remainder of the study.

https://doi.org/10.1021/acsami.2c09810
ACS Appl. Mater. Interfaces 2022, 14, 36143−36156

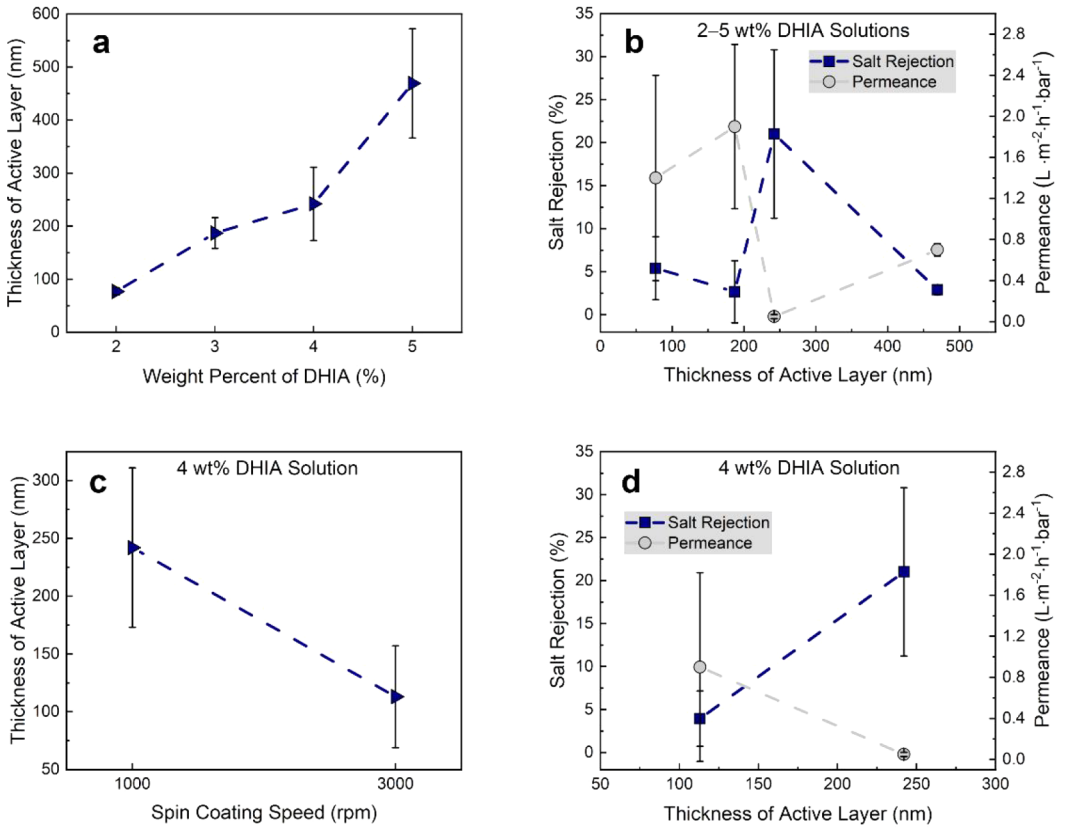

Figure 5. Properties of spin coated DHIA TFCs. (a) Correlation of active layer thickness to the weight percent of DHIA in solution when spin coated at 1000 rpm. Thickness was found by measuring cross sections of SEM images. (b) Salt rejection and water permeance of DHIA TFCs spin coated from 2 to 5 wt % DHIA solutions at 1000 rpm. (c) Effect of spin coating speed on the active layer thickness of a 4 wt % DHIA solution. (d) Salt rejection and water permeance of DHIA TFCs spin coated from 4 wt % DHIA solution at 1000 and 3000 rpm. All DHIA TFCs were tested with 2000 ppm of NaCl at 400 psi and pH 5.2 in dead-end mode. Dashed lines are provided as a guide to the eye.

2.4. DHIA TFC Fabrication and Performance. DHIA TFCs were initially fabricated by following the procedure used to prepare DHTA TFCs with the highest salt rejection (87.8%); that is, spin coating a 2 wt % DHIA solution onto a PSf at 1000 rpm and protonating the active layer in 1 M HCl. However, DHIA TFCs fabricated by using this procedure produced TFCs with poor salt rejection (<10%) and poor mechanical properties, as only one TFC could withstand the test pressure of 400 psi. Therefore, we extended the drying time to 24 h in an attempt to further densify the DHIA active layer and reduce the number of defects. Additionally, we used higher concentrations of DHIA in $NaOH/H_2O$ (3, 4, and 5 wt %) to determine if this would improve the salt rejection and mechanical properties of the DHIA active layer. As expected, the thickness of the active layer increased with increasing weight percent DHIA (Figure 5a).

The 2 wt % DHIA solution produced a 77 nm thick active layer with significant defects, as judged by the comparatively high water permeance (1.4 L m^{-2} h^{-1} bar^{-1}) and poor salt rejection (5.4%) (Figure 5a,b). DHIA TFCs spin coated from a 3 wt % solution also gave low salt rejection and water permeance values with high standard deviations, comparable to the 2 wt % solution. DHIA TFCs spin coated from 4 and 5 wt % DHIA solutions gave reproducible water permeance, though the 5 wt % solution showed lower salt rejection (2.9% vs 21.0%) (Figure 5b). We speculate that the 5 wt % solution gave lower salt rejection and higher water permeance, despite a thicker active layer than the 4 wt % solution, due to the defects that may have been formed during spin coating with a more viscous solution. Because initial experiments using 4 wt % DHIA solutions gave TFCs with the highest salt rejection (21.0%), this solution concentration was used to prepare DHIA TFCs for subsequent tests.

We then investigated the effect of the spin coating speed on the active layer thickness, salt rejection, and water permeance of DHIA TFCs made with a 4 wt % DHIA solution (Figure 5c,d). As expected, the increase in spin coating speed from 1000 to 3000 rpm produced a thinner DHIA active layer, with thickness decreasing from 242 to 113 nm, respectively (Figure 5c). The water permeance of the DHIA TFCs also scaled accordingly, with significantly higher permeance (0.9 L m^{-2} h^{-1} bar^{-1}) for DHIA TFCs spin coated at 3000 rpm as compared to those spin coated at 1000 rpm (0.06 L m^{-2} h^{-1} bar^{-1}) (Figure 5d). The salt rejection of DHIA TFCs spin coated at 3000 rpm was 3.9%. This may be a result of the significantly thinner active layer (113 nm) being more susceptible to transmembrane defects. In comparison, DHIA TFCs spin coated at 1000 rpm from a 4 wt % DHIA solution had an active layer thickness of 242 nm and reached a maximum salt rejection of 21.0%. These DHIA TFCs were chosen for additional characterization. We do note the large standard deviation in DHIA TFC performance (Figure 5b,d) despite testing several membranes. Regardless of the various processing parameters tried (such as modifying the substrate, changing drying temperature and times, adjusting the pH of both the polymer solution and acid bath, etc.; data not shown

https://doi.org/10.1021/acsami.2c09810
ACS Appl. Mater. Interfaces 2022, 14, 36143−36156

here), further improvements in performance were not achieved nor was the standard deviation reduced. Furthermore, we do note that the best salt rejection obtained for DHIA TFCs (29%) is still significantly lower than the best DHTA TFC (91%).

We also evaluated whether a DHTA TFC dried for a longer period of time (24 h, like DHIA TFCs) would perform significantly different from a DHTA TFC dried for 45 min. The water permeance of the 24 h dried DHTA TFC was lower (0.015 L m^{-2} h^{-1} bar^{-1}) but the NaCl rejection remained similar to that of DHTA TFCs dried for 45 min (80% rejection, with only one membrane prepared). Therefore, extended drying times did not improve the salt rejection of DHTA TFCs, unlike DHIA TFCs, which required longer drying times to achieve their highest salt rejection.

2.5. Comparison of Divalent Salt Rejection of DHTA and DHIA TFCs. DHTA and DHIA TFCs with the average salt rejections of NaCl, 87.8% and 21.0%, respectively, were chosen for all further characterization and analysis. Tests with larger divalent cations Mg^{2+} and Ca^{2+} and divalent polyatomic ion SO_4^{2-} revealed more details about the salt rejection abilities of DHTA and DHIA TFCs. TFCs were tested with 2000 ppm of NaCl, 500 ppm of $MgSO_4$, and 500 ppm of $CaCl_2$ single-salt solutions to emulate conditions used in characterizing commercial NF membranes.[47] Water permeance and salt rejection experiments were performed at pH 5.2. At this pH, the ionizable hydroxyl functionality, with a pK_a ~10, of the DHTA and DHIA polymer backbones is uncharged.[48] DHTA TFCs demonstrated high salt rejection of $MgSO_4$ and $CaCl_2$ (97.5 and 81.6%, respectively) while DHIA TFCs displayed low salt rejection of $MgSO_4$ and $CaCl_2$ (29.3 and 15.4%, respectively) (Figure 6). The poor salt rejection of DHIA agrees with other reports of non-crosslinked, nonlinear polyamides in the literature.[17,34] However, the maximum NaCl rejection of non-crosslinked, linear polyamides, without any additives, has been reported as ~40%.[34,36,37]

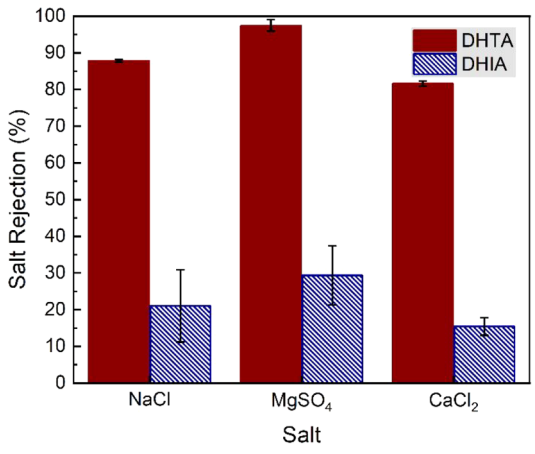

Figure 6. Salt rejection of DHTA and DHIA TFC membranes when tested with NaCl (2000 ppm), $MgSO_4$ (2000 ppm), and $CaCl_2$ (500 ppm) single-salt solutions at 400 psi and pH 5.2 in dead-end mode. DHTA TFCs were prepared by using a 2 wt % solution while DHIA TFCs were made by using a 4 wt % solution. DHTA and DHIA TFCs were fabricated by using the same procedure: spin coating at 1000 rpm for 1 min, protonation in 1 M HCl for 5 min, and drying at 60 °C. The final layer active layer thicknesses were 267 nm (DHTA) and 242 nm (DHIA).

Despite disparate salt rejections, DHTA and DHIA TFCs had similar water permeance, with DHTA showing a water permeance of 0.09 L m^{-2} h^{-1} bar^{-1} and DHIA displaying a slightly lower water permeance of 0.06 L m^{-2} h^{-1} bar^{-1}. One would expect to see higher water permeance paralleling the poor salt rejection of DHIA, following the empirical trade-off between water flux and salt rejection.[49] Moreover, DHIA's lower water permeance cannot be explained by a thicker active layer as the DHTA and DHIA thicknesses differed by less than 10%, with the DHTA layer being thicker (267 and 242 nm, respectively; thicknesses measured using SEM images of TFC cross sections). We then evaluated the surface and cross section properties of DHTA and DHIA TFCs to evaluate potential causes of the observed difference in membrane performance.

2.6. SEM Analysis. We investigated the morphologies of the DHTA and DHIA active layers using electron microscopy. At 25K magnification, SEM revealed that the DHTA TFC active layer was flat and without identifiable features (Figure 7a). Upon examination of the surface at higher magnification

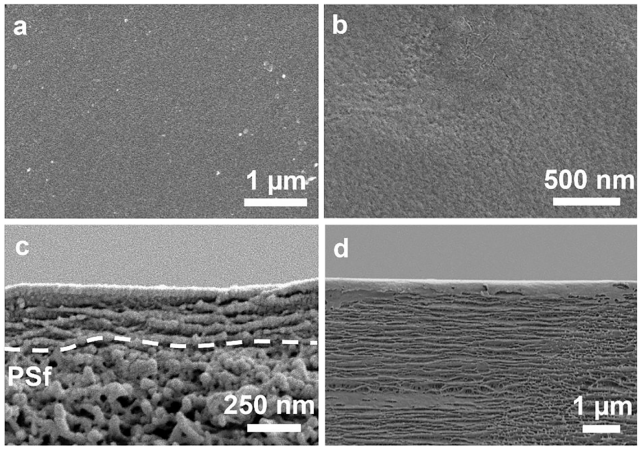

Figure 7. SEM images of DHTA TFC surface and cross section and DHTA bulk film cross section. DHTA TFC surface at (a) 25K magnification and (b) 45K magnification. Cross sections of (c) TFC at 60K magnification and (d) bulk film at 15K magnification.

(45K), DHTA appears to be somewhat textured but without any apparent pores or large defects (Figure 7b). As opposed to its unremarkable surface, the cross section of the DHTA active layer presents clear strata oriented parallel to the surface of the PSf substrate (Figure 7c). To understand if the stratified cross section morphology was an intrinsic property of DHTA or an effect of its thin-film nature or processing conditions, we also imaged a cross section of the bulk (10−20 μm thickness) film of DHTA (Figure 7d). Bulk films were prepared by doctor blading solutions of DHTA on a glass plate, which is a different processing method compared to the spin coating of active layers of TFCs. SEM distinctly shows that the layering or stratified structure seen in the spin coated active layer (~250 nm) (Figure 7c) is apparent in the bulk film as well (Figure 7d). This indicates that the stratified morphology of DHTA evident in Figure 7c,d is independent of the fabrication method used.

The surface of the DHIA TFC also appears featureless at 25K magnification (Figure 8a). At 45K magnification, the DHIA active layer seems to display small circular openings across the surface with larger openings measuring ~26 nm

https://doi.org/10.1021/acsami.2c09810
ACS Appl. Mater. Interfaces 2022, 14, 36143−36156

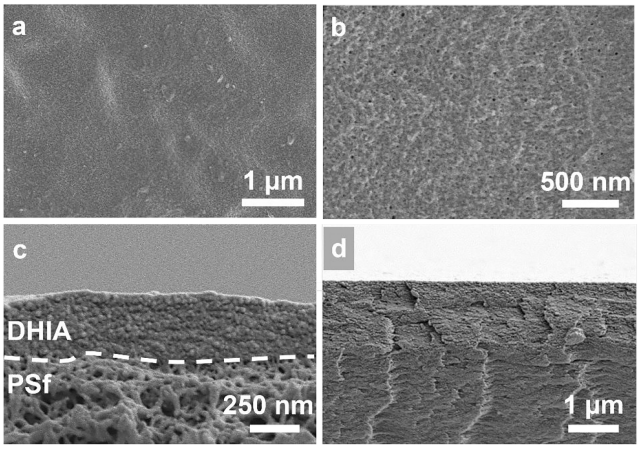

Figure 8. SEM images of DHIA TFC surface and cross section and DHIA bulk film cross section. DHIA TFC surface at (a) 25K magnification and (b) 45K magnification. Cross sections of (c) TFC at 60K magnification and (d) bulk film at 20K magnification.

across (Figure 8b). However, the openings do not appear to cross through the active layer, which is confirmed by Figure 8c. Furthermore, transmembrane pores with a diameter of 26 nm would promote high water permeance and zero rejection of monovalent and divalent ions. Hence, we may conclude that the openings are surface deep only. In contrast to the stratified cross section of DHTA consisting of alternating polymer layers, the DHIA active layer cross section exhibits an apparently dense cross section with no distinguishable stratification or porosity (Figure 8c). Examination of the DHIA bulk film cross section shows no strata either (Figure 8d), confirming that the observed dense cross section morphology of DHIA is independent of the fabrication method.

The contrasting structures may partially explain the differences in membrane performance. The stratified morphology of the DHTA TFC cross section might prevent defects in one stratum from percolating throughout the entirety of the active layer. DHIA, on the other hand, forms a dense active layer through which a defect could propagate more readily compared to a stratified morphology as seen in DHTA.

The stratification seen in the DHTA cross section (Figure 7c,d) is commonly observed in films prepared by using nematic solutions of rodlike polymers.[52−56] Here, because of viscosity considerations, an isotropic solution of 2 wt % DHTA is utilized for spin coating, well below the isotropic−nematic transition at 5 wt % DHTA in alkaline solutions. After spin coating at 1000 rpm, the DHTA concentration in the active layer increased to only ∼2.5 wt % and thus was still isotropic. Generally, surface anchoring will cause 2D rodlike molecules to preferentially orient themselves parallel to the casting surface (PSf) in the presence of an attractive interaction. However, anchoring effects weaken with increasing distance from the casting surface. When the spin coated active layer is immersed in the HCl coagulation bath, polymer−coagulant interfaces are formed throughout the active layer. The polymer−coagulant interfaces cause the 2D rodlike polymer to preferentially orient tangentially to this interface, which is also parallel to the casting surface (PSf). Further densification during the drying step due to affine deformation results in increased stratification.[57] Such stratification has also been observed in thin PPTA films formed by solution casting of an isotropic solution followed by coagulation.[58] In contrast, DHIA films do not exhibit a stratified morphology because DHIA chains cannot orient tangentially to the PSf surface during coagulation and drying due to their 3D isotropic structure (Figure 8c,d).

We also note here that the cross sections of DHTA and DHIA TFC active layers appear to be uniform throughout their thickness (i.e., regularly layered for DHTA and dense for DHIA). If we were to assume that the entire active layer formed a barrier to water permeance, we could normalize the water permeance according to the effective thickness of commercial polyamide RO and NF membranes, estimated to be ∼20 nm.[50,51] The normalized water permeances would then be 1.2 and 0.73 L m^{-2} h^{-1} bar^{-1} assuming a uniform active layer of 20 nm thickness for DHTA and DHIA TFCs, respectively.

2.7. WAXS Analysis. WAXS was used to analyze the in-plane orientation of DHTA and DHIA chains in the bulk films (stacks of 3−4 films measuring 20 μm thick each). The tests were performed such that the film surface normal is perpendicular to the X-ray beam (see Figure 9). 2D WAXS images reveal an anisotropic scattering pattern for DHTA whereas an isotropic scattering pattern is obtained for DHIA (Figure 9).

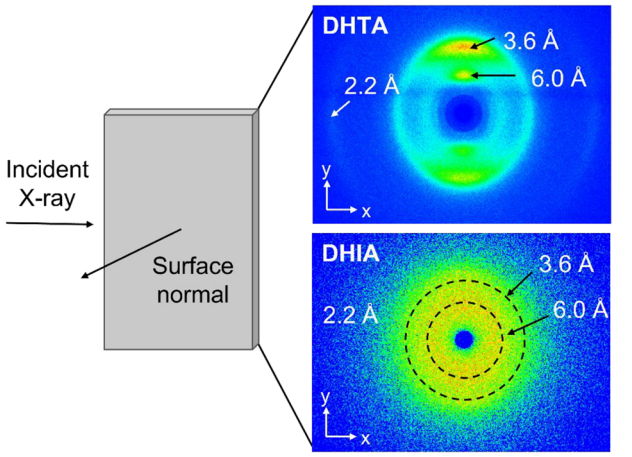

Figure 9. WAXS measurements of DHTA and DHIA bulk films. Illustration showing the direction of the X-ray beam with respect to the film surface normal and 2D scattering patterns of DHTA and DHIA. Distances associated with intramolecular periodicities are noted on the scattering patterns. The *x*- and *y*-axes are indicated in the lower left corner.

The anisotropic scattering patterns of DHTA indicate that DHTA chains adopt a uniplanar organization consistent with the stratified morphology observed in SEM. 1D lineouts of DHTA reveal Bragg peaks (2.2 and ∼6 Å) due to intramolecular periodicities, which are noted on the scattering patterns (Figures 9 and S6). In contrast, the 1D lineout of DHIA shows a broad hump of convoluted peaks centered around the same positions (i.e., 2.2 and ∼6 Å) (Figures 9 and S6). Such Bragg peaks—as opposed to broad amorphous halos—arise from orientation and possibly crystalline domains of rodlike DHTA. For both DHTA and DHIA, the average chain−chain, i.e., the intermolecular, distance is 3.6 Å (Figures 9 and S6). This interchain spacing agrees with other reports for fully aromatic, crosslinked polyamides.[16]

In summary, DHTA exhibits in-plane orientation that is evidenced by a stratified morphology in bulk films. Despite the

https://doi.org/10.1021/acsami.2c09810
ACS Appl. Mater. Interfaces 2022, 14, 36143−36156

Table 1. Swelling, Hydrophilicity, Roughness, and Charge of DHTA and DHIA Films

	water uptake[a] (wt %)	contact angle[b,c] (deg)	surface roughness[b,c,d] (nm)	% of −OH groups charged at[c]	
				pH 5.2	pH 10.6
DHTA	8.3 ± 1.4	35.3 ± 6.3	1.90	0	7.8 ± 1.1
DHIA	8.3 ± 1.5	32.3 ± 6.7	2.44	0.20 ± 0.10	8.8 ± 2.9

[a]Measured using bulk films (10−20 μm thick) of DHTA and DHIA. [b]Measurements taken at pH 5.2. [c]Measured on the active layer of TFCs. [d]RMS roughness of dry active layer surfaces.

lack of WAXS data for thin spin coated films, the similarity between SEM images of bulk and thin spin coated films strongly suggests that DHTA thin spin coated films also exhibit in-plane orientation. In contrast, DHIA, having a nonlinear, kinked backbone, does not show any in-plane orientation.

2.8. Hydrophilicity, Wettability, and Surface Characterization. While the cross section morphology and X-ray scattering of DHTA and DHIA TFCs and films offered insights into the factors contributing to the observed differences in membrane performance, we evaluated whether other commonly measured active layer properties had a role in these differences (Table 1).

2.8.1. Water Sorption. DHTA and DHIA TFCs demonstrated low pure water permeance despite swelling in water and showing a contact angle substantially less than 90°. Bulk films (10−75 μm thick) of both DHTA and DHIA absorbed a nontrivial amount of water upon reaching equilibrium: 8.3 wt % (Table 1). While bulk films may not perfectly reflect the behavior of the considerably thinner spin coated active layers of the TFCs (~250 nm), this measurement provides a reference point for the water uptake of DHTA and DHIA thin films. As both DHTA and DHIA absorbed the same amount of water, differences in water uptake did not contribute toward the observed differences in membrane performance.

2.8.2. Hydrophilicity. DHTA and DHIA spin coated active layers were shown to be hydrophilic, possessing contact angles of 35.3° and 32.2°, respectively (Table 1 and Figure S7).[59] The amide and hydroxyl groups of the DHTA and DHIA backbones enhance the hydrophilicity of the polymers, which contrasts with the fully aromatic backbone composed of hydrophobic benzene rings. One should note that while DHIA possesses a slightly lower contact angle compared to DHTA, the difference in contact angles is likely not significant enough to lead to a substantial difference in membrane performance. Other reports on the contact angles of commercial RO and NF membranes show that values differ by up to 6.4°, yet NaCl rejection differs by less than 3.1%.[60,61] Moreover, the slightly more hydrophilic DHIA TFCs displayed a slightly lower (albeit similar) permeance (0.06 L m^{-2} h^{-1} bar^{-1}) compared to DHTA TFCs (0.09 L m^{-2} h^{-1} bar^{-1}), which is contrary to the expected positive correlation between hydrophilicity and water permeance.[62] Therefore, we found no evidence suggesting that hydrophilicity was a significant contributor toward the observed differences in membrane performance between DHTA and DHIA TFCs.

2.8.3. Surface Roughness. Atomic force microscopy (AFM) measurements indicated similar surface roughness between DHTA and DHIA TFCs (Table 1 and Figure S8). In contrast to commonly used RO and NF TFCs that exhibit a RMS roughness ~10−125 nm, the DHTA and DHIA TFCs were considerably smoother.[10,63] Specifically, DHTA and DHIA TFCs displayed small and similar surface roughness values (2.44 and 1.90 nm, respectively) that were unlikely to have caused the observed differences in water permeance.

2.8.4. Surface Charge. X-ray photoelectron spectroscopy (XPS) measurements of Ag-probed membrane samples indicated that DHTA active layers were not charged at pH 5.2, whereas DHIA active layers were negligibly charged with 0.2% of all the possible hydroxyl or carboxylic groups deprotonated (Tables 1 and S2). Note that the polymer chains may have carboxylic acid end-groups that can contribute to the overall measured charge. However, we expect their contribution to be negligible as the concentration of these end-groups is low for high molecular weights of DHTA and DHIA. Even if the differences in membrane charge contributed toward the membrane properties, we would expect the more highly charged DHIA TFCs to exhibit greater salt rejection and/or permeance compared to DHTA TFCs.[64,65]

To confirm that our results were reliable, we repeated the experiment at pH 10.6 because the hydroxyl groups of the polymer backbones are similar in structure to phenol, which has a pK_a ~10.[48] By increasing the pH above the pK_a, we expected to see an increase in the number of charged hydroxyl groups, and indeed, we observed that the number of charged groups increased to 7.8% for DHTA TFCs and to 8.8% for DHIA TFCs (Tables 1 and S3). On average, around one hydroxyl group per six repeat units of DHTA or DHIA was deprotonated at pH 10.6 as depicted in Figure S9a. The NaCl rejection of both membranes increased at pH 10.6 compared with pH 5.2, with the average DHTA TFC rejection increasing from 87.8% to 92.7% while the DHIA TFC rejection improved from 21.0% to 31.7% (Figure S9b and Table S4). Likewise, the water permeance of each TFC increased when tested with the higher pH NaCl solution (Figure S9b). The increase in salt rejection and water permeance is consistent with expectations from the more negatively charged membrane surface (and therefore hydrophilicity).[64,65]

Overall, characterization of swelling, hydrophilicity, roughness, and charge of DHTA and DHIA TFCs revealed that these properties could not effectively explain the observed differences in membrane performance. Specifically, differences in any of these properties between DHTA and DHIA membranes were either small or contrary to expectations based on their performance. Only cross section imaging and X-ray scattering conveyed significant differences between DHTA and DHIA films in terms of their cross section morphology and polymer chain orientation.

2.9. PEG Rejection Experiments. With evidence of the structural differences of DHTA compared to DHIA, we endeavored to extract information about the pore size of DHTA and DHIA TFCs by measuring their PEG rejection. The PEG rejection curves are presented separately for each TFC sample instead of averaging the results. Duplicate membrane samples are arbitrarily labeled as 1 and 2. We used PEG molecular weights ranging from 200 to 2200 g mol^{-1} as NF membranes exhibit a molecular weight cutoff (MWCO) below 2000 g mol^{-1}. The two DHTA TFCs give reproducible results, demonstrating similar rejection for the range of PEG

https://doi.org/10.1021/acsami.2c09810
ACS Appl. Mater. Interfaces 2022, 14, 36143−36156

molecular weights tested, particularly from PEG 1383 to PEG 2220 (Figure 10). The rejection curves were fitted with a

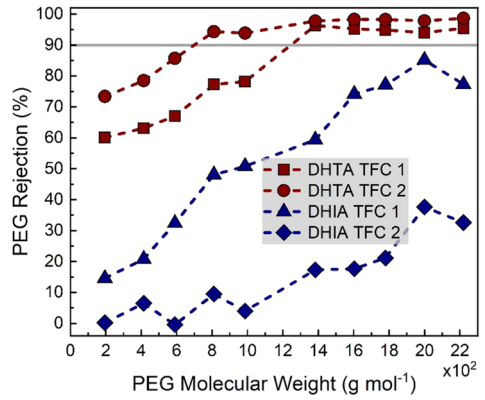

Figure 10. Rejection of PEG by DHTA and DHIA TFCs. DHTA/DHIA 1 and 2 refer to one of the duplicate TFCs. Results were not averaged as DHIA TFC1 and 2 displayed significantly different PEG rejections for each molecular weight. MWCO indicated by the intercept with the horizontal gray line at 90% rejection. Dashed lines are provided as a guide to the eye only.

fourth-order polynomial equation to estimate the PEG molecular weight at 90% rejection (section 7.3, Supporting Information). Solving the equations results in a MWCO of 1232 g mol^{-1} for DHTA TFC 1 and 734 g mol^{-1} for DHTA TFC 2 (Table S6).

Previous research by Lee et al. concludes that PEG diffuses through pores by its long axis, so that the length of the axis perpendicular to the membrane pore dictates whether PEG can or cannot diffuse through the pore.[66] The length of the perpendicular axis correlates to 2 times the hydrodynamic radius (r_h) of PEG, to within 1 Å, so that the membrane pore size can be approximated by using the PEG molecular weight closest to the calculated MWCO. PEG 1251 has an average calculated r_h of 1.1 nm, indicating that the average pore within the DHTA TFC 1 active layer possesses a diameter ~2.2 nm ($r_h \times 2$) (Table S7). PEG 723 possesses an average r_h of 0.83, suggesting that DHTA TFC 2 has an average pore size of 1.7 nm.

While DHTA TFC 1 and 2 display similar PEG rejections, DHIA 1 and 2 differ significantly, especially at PEG 590 and higher molecular weights. The rejection by DHIA TFC 1 and 2 is similarly low for PEG 194 and 414, indicating similar and relatively large pore radii for the smallest pores, possibly explaining why their salt rejections are comparable for the various salts tested (Figure 6). The rejection of each DHIA TFC then diverges, with the PEG rejection of DHIA TFC 1 increasing rapidly from PEG 590 to PEG 1999 and reaching a peak rejection of 85.1% for PEG 1999. DHIA TFC 2, on the other hand, displays a gradual increase in PEG rejection over the molecular range tested reaching a maximum of 37.6%. These results indicate that DHIA TFC 1 may have a lesser abundance of larger pores compared to DHIA TFC 2.

Though DHIA TFC 1 did not exhibit a MWCO in the data collected, we fit its PEG rejection curve with a fourth-order polynomial equation to estimate the MWCO as its maximum PEG rejection of 85.1% was close to 90% (Figure S10). The rejection curve of DHIA TFC 2, however, was not fitted with a fourth-order polynomial to estimate the MWCO as its maximum PEG rejection was only 37.6%, and the extrapolation of rejection to 90% may not have accurately reflected real-life data. We estimated the MWCO to be 2070 g mol^{-1} for DHIA TFC (Table S6). The hydrodynamic radii of the closest PEG MW (2088 g mol^{-1}) were calculated to give an average r_h of 1.5 nm (Table S7). Thus, the average pore size of DHIA TFC 1 can be estimated to be around 3.0 nm. This value is greater than those found for DHTA TFC samples (2.2 and 1.7 nm).

For reference, the pore sizes of NF membranes are generally ~1−2 nm.[6,67] Pore size values stated in the literature for NF membranes vary widely—with ranges from ~0.4 to 1.6 nm and conflicting reports for the same commercially available membranes—based on the details of the experimental methodology and analyses utilized.[68,69] In summary, DHTA TFCs have an average pore size that allows them to be used for NF applications whereas DHIA TFCs have average pore sizes larger than those necessary for NF applications.

3. CONCLUSIONS

The backbone geometry of aromatic polyamides is an important parameter when designing thin film composites (TFCs) for salt exclusion applications. We found that membranes fabricated from the linear, rigid, rodlike polymer poly(3,3′-dihydroxybenzidine terephthalamide) (DHTA) exhibit significantly higher average salt rejection of NaCl (87.8%), $MgSO_4$ (97.5%), and $CaCl_2$ (81.6%) when compared with membranes fabricated from the chemically identical but nonlinear semirigid analogue poly(3,3′-dihydroxybenzidine isophthalamide) (DHIA), which displays average rejection values of 21.0, 29.3, and 15.4% for the same salts. Differences in viscosities of DHTA and DHIA solutions for spin coating led to the need for different polymer processing conditions to obtain thin film membranes. SEM cross sections of resulting DHTA and DHIA TFCs and bulk films reveal stark differences in the microstructure of DHTA and DHIA active layers, where DHTA shows a distinct stratified morphology whereas DHIA exists as a featureless dense layer. WAXS measurements confirmed that DHTA polymer chains exhibit uniplanar orientation while DHIA polymer chains show no uniplanar orientation due to their 3D isotropic structure. The differences in observed membrane performance cannot be explained by differences in bulk water uptake, contact angle, surface roughness, or surface charge between DHTA or DHIA. PEG rejection experiments confirm that differences exist at a nanoscale level between DHTA and DHIA, with the DHTA active layers exhibiting an average pore size of ~2 nm compared to an average pore size of ~3 nm in DHIA active layers. These results demonstrate that the polymer backbone geometry is indeed an import design parameter. When changing the backbone from a semirigid geometry to a linear, rodlike geometry, membranes can be prepared that are characterized by a stratified morphology with in-plane orientation of the polymer chains. This work shows that membranes that exhibit such morphologies are promising desalting membranes.

4. EXPERIMENTAL SECTION

4.1. Materials. All materials were used as received unless otherwise noted. 3,3′-Dihydroxybenzidine (HAB, 99%) was purchased from TCI America, Inc. Calcium chloride ($CaCl_2$, anhydrous, 96%), terephthaloyl chloride (TPC, flakes, 99%) and isophthaloyl chloride (IPC, flakes, 99%) were acquired from Sigma-Aldrich. TPC and IPC were sublimed at 80 °C and stored under nitrogen before use. NMP (extra dry over molecular sieves, 99.5%) was purchased

https://doi.org/10.1021/acsami.2c09810
ACS Appl. Mater. Interfaces 2022, 14, 36143−36156

from Acros Organics. HCl (ACS plus, 36.5−38 wt %) and NaOH solution (50/50 w/w %) were purchased from VWR International. The polysulfone (PSf) support layer with polypropylene (PP) backing (PS-20 GPP) used for preparing the TFC membranes was kindly donated by Solecta, Inc. (Oceanside, CA). Sodium chloride (NaCl), magnesium sulfate ($MgSO_4$), and calcium chloride ($CaCl_2$) for salt rejection measurements were purchased from Alfa Aesar, Mallinckrodt Pharmaceuticals, and Fisher Scientific, respectively. Poly(ethylene glycol) (PEG, analytical standard) 200, 400, 600, and 1000 g mol^{-1} for MWCO experiments were sourced from Agilent. PEG (2000 g mol^{-1}, analytical standard) was sourced from Sigma-Aldrich.

4.2. Polymer Synthesis. *4.2.1. Poly(3,3′-dihydroxybenzidine terephthalamide) (DHTA).* The synthesis of DHTA was adapted from the method described by Chokai et al.[31] Briefly, 165 mL of anhydrous NMP and 8.2 g of dried $CaCl_2$ (80.2 mmol) were added under nitrogen to a flame-dried, 500 mL three-neck round-bottom flask equipped with an overhead stirrer and nitrogen inlet. The flask was gently heated until all the $CaCl_2$ dissolved and then cooled, and next 5.50 g (25.4 mmol) of HAB was added at room temperature (∼22 °C). The flask was submerged in a NaCl/ice bath (T_{bath} < 0 °C) for 20 min before being charged with 5.16 g (25.4 mmol) of TPC. The mixture was then vigorously stirred at 2000 rpm for 1 h at subzero temperatures to yield a highly viscous solution. The ice bath was removed after 1 h, and the stirring speed decreased to 1000 rpm. After overnight stirring at room temperature, the viscous polymer solution was precipitated in deionized (DI) water to yield long, yellow fibrous precipitate, which are indicative of high molecular weight polymer. The product was washed in DI water (3 L, three times), filtered, and dried under vacuum at 110 °C for 24 h. The polymer product was obtained with a 99% yield (8.75 g).

4.2.2. Poly(3,3′-dihydroxybenzidine isophthalamide) (DHIA). The procedure for DHIA follows that of DHTA, except 5.16 g (25.4 mmol) of IPC was used instead of TPC. The DHIA reaction solution exhibited lower viscosity compared to the DHTA reaction solution but still formed thin, beige fibrous polymer precipitates in DI water. The polymer was dried under vacuum at 110 °C for 24 h after washing. The polymer product was obtained with a 94% yield (8.28 g).

4.3. Fabrication of DHTA and DHIA TFCs. *4.3.1. PSf Support.* The PSf support used as a structural backing for TFCs was rinsed with ethanol and DI water to remove the preservative coating, cut into circular coupons (diameter: 6.75 cm), and immersed in DI water for 24 h before use. DHTA and DHIA were dissolved by using a solution of NaOH in DI water as the hydroxide ion of NaOH deprotonates the hydroxyl (−OH) groups along the backbone of DHTA and DHIA.

4.3.2. DHTA TFC Fabrication. We chose a 2 wt % polymer solution of DHTA in $NaOH/H_2O$ for spin coating because higher concentrations resulted in solutions too viscous for spin coating. The amount of NaOH was fixed at 2.5 mol equiv of DHTA and dissolved in DI water over 24 h, with 2 h heating at 65 °C, to give a viscous, dark brown solution. This solution containing charged DHTA was centrifuged at 5000 rpm for 10 min to remove any particulates prior to spin coating. PSf circular coupons were patted dry with a KimWipe, taped onto a round plastic plate, and vacuum-sealed in place on the spin coater. DHTA solution was dropped onto the PSf coupon, allowed to spread until the surface was fully covered in a static dispense, and then allowed to soak into the PSf for 6 min total. The DHTA-PSf was spin coated for 1000 or 3000 rpm for 1 min. Immediately after spin coating, the DHTA TFC was placed in a 1 or 0.001 M HCl bath (5 min) to protonate the phenoxides back to hydroxyl groups and insolubilize the active layer. After protonation, the DHTA TFC was immersed in a LGW bath (10 min), helping to swell the active layer, before being moved back to the acid bath to ensure that all phenoxides had been protonated (2 min). A final rinse in the LGW bath (3 min) to remove excess HCl preceded drying the DHTA TFC for 45 min at 60 °C in the oven.

4.3.3. DHIA TFC Fabrication. A 4 wt % DHIA solution was chosen based on ease of processing and the ability to obtain reproducible membranes. DHIA was dissolved by using 1.1 mol equiv of NaOH in DI water to form a 4 wt % solution. This solution was dropped onto the PSf coupon surface, allowed to spread until the PSf surface was fully covered, and then allowed to soak into the PSf for 6 min total before being spin coated at 1000 or 3000 rpm for 1 min. The DHIA layer was protonated by using 1 M HCl (5 min). Only 1 M HCl was used for protonating the DHIA active layer after spin coating as initial experiments indicated that weaker acids (i.e., 0.1 M HCl) caused the active layer to detach from the PSf substrate. The DHIA TFC was then soaked in LGW (10 min). The DHIA TFC underwent a final soak in 1 M HCl (2 min) before rinsing with LGW (3 min). The membranes were then dried at 60 °C in the oven.

4.4. Polymer Characterization Techniques. FTIR spectra on DHTA and DHIA powders were collected by using a PerkinElmer Spectrum spectrometer between 4000 and 750 cm^{-1} at 1 cm^{-1} resolution. ^1H NMR analyses were performed with DHTA samples dissolved in a solution (20:1 by volume) of DMSO-d_6 and 40 wt % sodium deuteroxide NaOD in D_2O and filtered through a 0.44 μm Nylon filter. DHIA ^1H NMR samples were dissolved by using DMSO-d_6. Samples for ^1H NMR were run on a Bruker AVANCE III Nanobay 400 MHz NMR spectrometer. The molecular weights of DHIA and DHTA were found using SEC. DHTA and DHIA were measured against polystyrene standards in NMP with 30 mM LiBr and H_3PO_4 as the mobile phase. Thermogravimetric analysis (TGA 5500, TA Instruments) of DHTA and DHIA was performed over a temperature range of 25−600 °C by using a 10 °C min^{-1} temperature ramp, with an isothermal hold at 120 °C for 30 min to remove water.

4.5. Membrane Characterization Techniques. *4.5.1. Imaging and Surface Roughness.* SEM imaging was performed by using a Hitachi S-4700 cold cathode field emission SEM operating at an accelerating voltage of 2.0 kV and a working distance between 11.5 and 12.5 mm. For surface images, intact TFC membranes were dried at room temperature. Cross sections were prepared by taking the wet DHTA or DHIA TFC membrane, making an incision with a razor blade on the polypropylene backing, and carefully peeling off the polypropylene. The DHTA/DHIA-PSf composite was then placed in liquid nitrogen and freeze-fractured. Bulk film (10−20 μm) cross sections of DHTA and DHIA were freeze fractured similarly. Surface and cross section samples were sputter-coated (Cressington 108 Auto) with a 4−5 nm layer of Au−Pd before imaging. Cross section thicknesses were found by using ImageJ software (freely sourced Java software from https://imagej.nih.gov/). The cross section in four images was measured from the interface of the DHTA/DHIA active layer and PSf to the top of the DHTA/DHIA active layer, with four measurements per image. Duplicate membrane samples were measured for DHTA and DHIA TFCs with the highest average salt rejection. The thicknesses reported here reflect the average ± standard deviation of those measurements. AFM topological maps were obtained by using an Asylum Research MFP3D atomic force microscope (Figure S8). The surfaces of DHTA and DHIA TFCs were mapped by using 512 scan lines at a scan rate of 0.5 Hz over an area of 6.3 μm^2. The surface roughness was found by calculating the root-mean-square roughness from 262144 points.

4.5.2. Hydrophilicity and Wettability. Water uptake (WU) measurements of DHTA and DHIA were performed on two bulk films of each polymer (3.2 cm in diameter, 10−75 μm thick) with five measurements per film. Films were placed in DI water for 48 h before being gently patted dry with a KimWipe. Films were massed gravimetrically and then dried at 60 °C overnight in air. The following equation was used to calculate the water uptake:

$$\mathrm{WU} = \frac{m_w - m_d}{m_d} \times 100\ \mathrm{wt}\ \% \quad (1)$$

where m_w is the mass of the wet film and m_d is the mass of the dried film. Contact-angle measurements were performed by using the captive bubble method described in the literature.[60] A small section of DHTA or DHIA TFC was taped to a glass slide and then immersed with the active layer face down in DI water. A 10 μL air bubble was deposited onto the surface of the active layer, and an image was taken within 30 s of bubble attachment by using a ramé-hart goniometer/tensiometer equipped with DROPimage Pro. Five images were taken

https://doi.org/10.1021/acsami.2c09810
ACS Appl. Mater. Interfaces 2022, 14, 36143−36156

of each membrane and results averaged across duplicate membrane samples per polymer (10 measurements total). ImageJ software with the Contact Angle plugin was used to analyze the images. The drop and surface were outlined by hand using the manual points procedure. The reported contact angles were calculated based on an elliptically shaped drop, as this was the shape that most closely matched that of the drop by sight.

4.5.3. Surface Charge. Membrane surface charge was found by measuring the concentration of silver counterions in the active layer, a technique adapted from that described by Coronell et al.[70] Silver nitrate ($AgNO_3$) solutions at concentrations of 40 and 1 μM were prepared at pH 5.2. A 3 × 3 cm^2 square was removed from the center of a wet DHTA and DHIA TFCs, gently dried with a KimWipe, and placed with the active layer face down in the 40 μM $AgNO_3$ solution for 10 min, allowing Ag^+ to bind to deprotonated hydroxyl groups or carboxylic acids in the active layer. The membrane square was removed and gently dried by using filter paper, and the process was repeated with fresh 40 μM $AgNO_3$ solution. The square was then placed in 1 μM $AgNO_3$ for 7 min. The square was removed, dried, and placed in fresh 1 μM $AgNO_3$ solution three more times, removing unbound Ag^+ ions. The experiment was repeated for $AgNO_3$ solutions at pH 10.6. Membrane squares were dried overnight at room temperature before performing measurements using XPS (Kratos Analytical Axis Ultra Delay-Line Detector, Kratos Analytical Inc.). Additional details on the instrument and method can be found in the Supporting Information (section 6). The Ag atomic composition was compared to the N atomic composition to quantify the amount of Ag in the top ~7 nm of the active layer. WAXS measurements of DHTA and DHIA bulk films (stacks of 3−4 films with thicknesses of 20 μm each) were taken by using a Rigaku SmartLab diffractometer equipped with a HyPix-3000 2D detector and a Cu Kα radiation source. DHTA and DHIA film samples were mounted 27 mm away from the detector with their surface normal perpendicular to the incident X-ray beam direction and exposed for 10 min.

4.5.4. High-Performance Liquid Chromatography Selected Reaction Monitoring Tandem Mass Spectrometry (HPLC-SRM-MS/MS). HPLC-SRM-MS/MS analysis enabled the separation and quantification of individual PEG molecular weights for determination of membrane MWCO. The prepared samples (10 μL injection volume) were analyzed by HPLC-SRM-MS/MS using an Accela 600 HPLC coupled with TSQ Quantum Ultra mass spectrometry (Thermo Fisher Scientific). An Acquity UPLC HSS T3 Column (SKU: 186003539, Waters) was used for the separation of PEG molecular weights. LC gradients were performed at a flow rate of 300 μL/min by using 0.1% formic acid in water (solvent A) and acetonitrile (solvent B). Additional experimental details regarding the gradients used can be found in the Supporting Information (section 7). The HESI ion source was used for ionization with 3.5 kV spray voltage, sheath gas pressure of 30 units, ion sweep gas pressure of 1 unit, auxiliary gas pressure of 25 units, and capillary temperature of 225 °C. The target product ions of 89.1 and 133.1 were monitored for PEG targets with different ion types and molecular weights (Table S5). The Q1 and Q3 resolutions were both set to 0.7 with a dwell time of 0.05 s for each transition in the triple quadrupole mass spectrometry. Herein, Q1 (first quadrupole) was used to select target m/z precursor ion for further fragmentation in the Q2 collision cell (second quadrupole); Q3 (third quadrupole) was then used to selectively monitor target product ions generated from Q2. One transition referred to a pair of precursor ion/product ion for monitoring. Quantifications of each PEG targets were based on the peak area of those two transitions by using the Qual Browser in Xcalibur 4.3.73.11 (Thermo Fisher Scientific).

4.6. Membrane Performance. A stainless-steel stirred cell (Sterlitech HP4750) was used to determine each TFC membrane performance in terms of salt and PEG rejection and water permeance. The cell has an active membrane area of 14.6 cm^2. Circular membrane coupons for filtration experiments were cut out by using a punch die with a diameter of 1.875 in. (4.76 cm) (McMaster-Carr). Salt rejection and water permeance experiments were performed in dead-end mode by using salt solutions prepared with LGW. The cell was stirred at 350 rpm to minimize the effects of concentration polarization; the relatively low water flux of the membranes studied also contributed to minimizing concentration polarization (CP). All membranes were evaluated under the same stirring conditions (that minimized CP), which enabled valuable comparisons of performance across membranes. DHTA and DHIA TFC membranes were compacted in LGW overnight (~20 h) by using the same filtration system and pressure (400 psi) used during filtration tests. The membranes were then compacted for ~2 h with the salt solution of interest until a steady state had been reached (i.e., constant permeance and salt rejection). Two duplicate membranes samples were measured for each membrane performance data point. The pure water permeance A (L m^{-2} h^{-1} bar^{-1}) was determined by collecting samples over a 25 min period after a steady state had been reached (i.e., after the initial 20 h of the compaction run and the additional 2 h of stabilization during the filtration run). The samples were weighed, and the volume found by using density. Equation 2 was used to find the water permeance, where ΔV is the volume of permeate water, Δt is the time over which ΔV eluted, d is the effective membrane area, and ΔP is the transmembrane pressure.

$$A = \frac{\Delta V}{\Delta t \times d \times \Delta P} \tag{2}$$

We used 2000 ppm of NaCl, 2000 ppm of $MgSO_4$, and 500 ppm of $CaCl_2$ single-salt solutions to investigate the salt rejection performance of the TFCs as these concentrations are used to assess the properties of commercial NF membranes.[47] The TFCs were subjected to an applied pressure of 400 psi at room temperature (~22 °C) and pH 5.2. A conductivity probe (Fisher Scientific Accumet XL60 dual channel pH/mV/ion/conductivity meter) measured the conductivity of the feed and permeate solutions to determine the salt rejection R as given by

$$R = \left(1 - \frac{c_p}{c_f}\right) \times 100\% \tag{3}$$

where c_f is the conductivity of the feed solution and c_p is the conductivity of the permeate. For determining MWCO, stock solutions of PEG 200, 400, 600, 1000, and 2000 g mol^{-1} were separately prepared at concentrations of 200 ppm in LGW. LC-SRM-MS/MS determined the concentration of PEG in the permeate and feed solutions. The rejection of PEG was found by using eq 3, with peak area (concentration) as a substitute for conductivity.

■ ASSOCIATED CONTENT

Supporting Information

The Supporting Information is available free of charge at https://pubs.acs.org/doi/10.1021/acsami.2c09810.

FTIR and NMR spectra; molecular weight measurements; thermogravimetric analysis; correlation of protonation time to membrane properties; WAXS 1D lineouts; contact angle measurements; AFM images; XPS tabulated atomic concentrations; effect of pH on salt rejection and permeance; LC-SRM-MS/MS experimental details; PEG rejection curve fitting; PEG hydrodynamic radius calculations (PDF)

■ AUTHOR INFORMATION

Corresponding Authors

Orlando Coronell − *Department of Environmental Sciences and Engineering, Gillings School of Global Public Health, The University of North Carolina at Chapel Hill, Chapel Hill, North Carolina 27599-7431, United States;* orcid.org/0000-0002-7018-391X; Email: coronell@unc.edu

https://doi.org/10.1021/acsami.2c09810
ACS Appl. Mater. Interfaces 2022, 14, 36143−36156

Theo J. Dingemans − *Department of Applied Physical Sciences, The University of North Carolina at Chapel Hill, Chapel Hill, North Carolina 27599-3050, United States;* orcid.org/0000-0002-8559-2783; Email: tjd@unc.edu

Authors

Anna C. Fraser − *Department of Applied Physical Sciences, The University of North Carolina at Chapel Hill, Chapel Hill, North Carolina 27599-3050, United States*

Nick Guan Pin Chew − *Department of Environmental Sciences and Engineering, Gillings School of Global Public Health, The University of North Carolina at Chapel Hill, Chapel Hill, North Carolina 27599-7431, United States;* orcid.org/0000-0001-7634-537X

Maruti Hegde − *Department of Applied Physical Sciences, The University of North Carolina at Chapel Hill, Chapel Hill, North Carolina 27599-3050, United States*

Fei Liu − *Department of Environmental Sciences and Engineering, Gillings School of Global Public Health, The University of North Carolina at Chapel Hill, Chapel Hill, North Carolina 27599-7431, United States;* orcid.org/0000-0001-9952-2922

Chih-Wei Liu − *Department of Environmental Sciences and Engineering, Gillings School of Global Public Health, The University of North Carolina at Chapel Hill, Chapel Hill, North Carolina 27599-7431, United States;* orcid.org/0000-0002-0823-0252

Complete contact information is available at: https://pubs.acs.org/10.1021/acsami.2c09810

Notes

The authors declare no competing financial interest.

ACKNOWLEDGMENTS

We thank Carrie Donley for performing XPS measurements and interpreting the XPS results, Amar Kumbhar for imaging our samples with AFM and for helping with interpretation, and Zhenfa Zhang for help with HPLC-MS measurements. We thank Keisuke Saito and Jiawanjun Meredith Shi from Rigaku for providing 2D WAXS measurements of our materials. We thank Solecta, Inc., for kindly providing us with the PSf-PP support layer (PS-20 GPP). This material is based upon work supported by the National Science Foundation Graduate Research Fellowship under Grant DGE-1650116 and the National Institute of Environmental Health Sciences (NIEHS) (P42ES031007). This work was also supported in part by the Creativity Hubs Program of the University of North Carolina at Chapel Hill. SEM, XPS, and AFM were performed at the Chapel Hill Analytical and Nanofabrication Laboratory, CHANL, a member of the North Carolina Research Triangle Nanotechnology Network, RTNN, which is supported by the National Science Foundation, Grant ECCS-1542015, as part of the National Nanotechnology Coordinated Infrastructure, NNCI. We thank the University of North Carolina's Department of Chemistry NMR Core Laboratory for the use of their NMR spectrometers, which is supported by the National Science Foundation under Grant CHE-0922858. Any opinions, findings, and conclusions or recommendations expressed in this material are those of the author(s) and do not necessarily reflect the views of the National Science Foundation or NIEHS.

REFERENCES

(1) Greenlee, L. F.; Lawler, D. F.; Freeman, B. D.; Marrot, B.; Moulin, P. Reverse Osmosis Desalination: Water Sources, Technology, and Today's Challenges. *Water Res.* **2009**, *43* (9), 2317−2348.

(2) Al-Karaghouli, A.; Kazmerski, L. L. Energy Consumption and Water Production Cost of Conventional and Renewable-Energy-Powered Desalination Processes. *Renew. Sustain. Energy Rev.* **2013**, *24*, 343−356.

(3) Lee, A.; Elam, J. W.; Darling, S. B. Membrane Materials for Water Purification: Design, Development, and Application. *Environ. Sci. Water Res. Technol.* **2016**, *2* (1), 17−42.

(4) Ziolkowska, J. R. Desalination Leaders in the Global Market − Current Trends and Future Perspectives. *Water Supply* **2016**, *16* (3), 563−578.

(5) Lee, K. P.; Arnot, T. C.; Mattia, D. A Review of Reverse Osmosis Membrane Materials for Desalination—Development to Date and Future Potential. *J. Membr. Sci.* **2011**, *370* (1), 1−22.

(6) Yang, Z.; Zhou, Y.; Feng, Z.; Rui, X.; Zhang, T.; Zhang, Z. A. Review on Reverse Osmosis and Nanofiltration Membranes for Water Purification. *Polymers* **2019**, *11* (8), 1252.

(7) Paul, M.; Jons, S. D. Chemistry and Fabrication of Polymeric Nanofiltration Membranes: A Review. *Polymer* **2016**, *103*, 417−456.

(8) Cadotte, J. E.; Petersen, R. J.; Larson, R. E.; Erickson, E. E. A New Thin-Film Composite Seawater Reverse Osmosis Membrane. *Desalination* **1980**, *32*, 25−31.

(9) Petersen, R. J. Composite Reverse Osmosis and Nanofiltration Membranes. *J. Membr. Sci.* **1993**, *83* (1), 81−150.

(10) Lin, L.; Feng, C.; Lopez, R.; Coronell, O. Identifying Facile and Accurate Methods to Measure the Thickness of the Active Layers of Thin-Film Composite Membranes − A Comparison of Seven Characterization Techniques. *J. Membr. Sci.* **2016**, *498*, 167−179.

(11) Coronell, O.; Mariñas, B. J.; Cahill, D. G. Depth Heterogeneity of Fully Aromatic Polyamide Active Layers in Reverse Osmosis and Nanofiltration Membranes. *Environ. Sci. Technol.* **2011**, *45* (10), 4513−4520.

(12) Ghosh, A. K.; Jeong, B.-H.; Huang, X.; Hoek, E. M. V. Impacts of Reaction and Curing Conditions on Polyamide Composite Reverse Osmosis Membrane Properties. *J. Membr. Sci.* **2008**, *311* (1−2), 34−45.

(13) Khorshidi, B.; Thundat, T.; Fleck, B. A.; Sadrzadeh, M. A Novel Approach Toward Fabrication of High Performance Thin Film Composite Polyamide Membranes. *Sci. Rep.* **2016**, *6*, 22069.

(14) Khorshidi, B.; Thundat, T.; Fleck, B. A.; Sadrzadeh, M. Thin Film Composite Polyamide Membranes: Parametric Study on the Influence of Synthesis Conditions. *RSC Adv.* **2015**, *5* (68), 54985−54997.

(15) Shi, M.; Yan, W.; Dong, C.; Liu, L.; Xie, S.; Gao, C. Solvent Activation before Heat-Treatment for Improving Reverse Osmosis Membrane Performance. *J. Membr. Sci.* **2020**, *595*, 117565.

(16) Ali, Z.; Wang, Y.; Ogieglo, W.; Pacheco, F.; Vovusha, H.; Han, Y.; Pinnau, I. Gas Separation and Water Desalination Performance of Defect-Free Interfacially Polymerized Para-Linked Polyamide Thin-Film Composite Membranes. *J. Membr. Sci.* **2021**, *618*, 118572.

(17) Juhn Roh, I. Effect of the Physicochemical Properties on the Permeation Performance in Fully Aromatic Crosslinked Polyamide Thin Films. *J. Appl. Polym. Sci.* **2003**, *87* (3), 569−576.

(18) Mohammad, A. W.; Teow, Y. H.; Ang, W. L.; Chung, Y. T.; Oatley-Radcliffe, D. L.; Hilal, N. Nanofiltration Membranes Review: Recent Advances and Future Prospects. *Desalination* **2015**, *356*, 226−254.

(19) Ridgway, H. F.; Orbell, J.; Gray, S. Molecular Simulations of Polyamide Membrane Materials Used in Desalination and Water Reuse Applications: Recent Developments and Future Prospects. *J. Membr. Sci.* **2017**, *524*, 436−448.

(20) Geise, G. M. Why Polyamide Reverse-Osmosis Membranes Work so Well. *Science* **2021**, *371* (6524), 31−32.

(21) Culp, T. E.; Khara, B.; Brickey, K. P.; Geitner, M.; Zimudzi, T. J.; Wilbur, J. D.; Jons, S. D.; Roy, A.; Paul, M.; Ganapathysubramanian, B.; Zydney, A. L.; Kumar, M.; Gomez, E.

D. Nanoscale Control of Internal Inhomogeneity Enhances Water Transport in Desalination Membranes. *Science* **2021**, *371* (6524), 72−75.
(22) Pacheco, F.; Sougrat, R.; Reinhard, M.; Leckie, J. O.; Pinnau, I. 3D Visualization of the Internal Nanostructure of Polyamide Thin Films in RO Membranes. *J. Membr. Sci.* **2016**, *501*, 33−44.
(23) Fujioka, T.; O'Rourke, B. E.; Michishio, K.; Kobayashi, Y.; Oshima, N.; Kodamatani, H.; Shintani, T.; Nghiem, L. D. Transport of Small and Neutral Solutes through Reverse Osmosis Membranes: Role of Skin Layer Conformation of the Polyamide Film. *J. Membr. Sci.* **2018**, *554*, 301−308.
(24) Dennison, J. M.; Xie, X.; Murphy, C. J.; Cahill, D. G. Density, Elastic Constants, and Thermal Conductivity of Interfacially Polymerized Polyamide Films for Reverse Osmosis Membranes. *ACS Appl. Nano Mater.* **2018**, *1* (9), 5008−5018.
(25) Lin, L.; Lopez, R.; Ramon, G. Z.; Coronell, O. Investigating the Void Structure of the Polyamide Active Layers of Thin-Film Composite Membranes. *J. Membr. Sci.* **2016**, *497*, 365−376.
(26) Xu, J.; Yan, H.; Zhang, Y.; Pan, G.; Liu, Y. The Morphology of Fully-Aromatic Polyamide Separation Layer and Its Relationship with Separation Performance of TFC Membranes. *J. Membr. Sci.* **2017**, *541*, 174−188.
(27) Culp, T. E.; Shen, Y.; Geitner, M.; Paul, M.; Roy, A.; Behr, M. J.; Rosenberg, S.; Gu, J.; Kumar, M.; Gomez, E. D. Electron Tomography Reveals Details of the Internal Microstructure of Desalination Membranes. *Proc. Natl. Acad. Sci. U. S. A.* **2018**, *115* (35), 8694−8699.
(28) Kłosowski, M. M.; McGilvery, C. M.; Li, Y.; Abellan, P.; Ramasse, Q.; Cabral, J. T.; Livingston, A. G.; Porter, A. E. Micro-to Nano-Scale Characterisation of Polyamide Structures of the SW30HR RO Membrane Using Advanced Electron Microscopy and Stain Tracers. *J. Membr. Sci.* **2016**, *520*, 465−476.
(29) Peng, L. E.; Yao, Z.; Yang, Z.; Guo, H.; Tang, C. Y. Dissecting the Role of Substrate on the Morphology and Separation Properties of Thin Film Composite Polyamide Membranes: Seeing Is Believing. *Environ. Sci. Technol.* **2020**, *54* (11), 6978−6986.
(30) Vickers, R.; Weigand, T. M.; Miller, C. T.; Coronell, O. Molecular Methods for Assessing the Morphology, Topology, and Performance of Polyamide Membranes. *J. Membr. Sci.* **2022**, *644*, 120110.
(31) Chokai, M.; Wilbers, D.; Nagasaka, B.; Kuwahara, H.; de Weijer, T.; Klop, E.; Hayakawa, T.; Kakimoto, M. Development of a Highly Oriented Poly-Biphenylenebisoxazole Fiber Obtained via a Precursor Polymer Spun From a Liquid Crystalline Aqueous Solution. *Polym. J.* **2009**, *41* (8), 679−684.
(32) Kang, C. S.; Park, C. W.; Jee, M. H.; Paik, M. J.; Baik, D. H. Synthesis and Thermal Properties of Polyhydroxyamide Copolymer and Its Derivatives. *Fibers Polym.* **2016**, *17* (5), 657−662.
(33) Chang, J.-H.; Farris, R. J. Characterization of Two Precursor Polyblends: Polyhydroxyamide and Poly(Amic Acid). *Polym. Eng. Sci.* **2000**, *40* (2), 320−329.
(34) Kwak, S.-Y. Relationship of Relaxation Property to Reverse Osmosis Permeability in Aromatic Polyamide Thin-Film-Composite Membranes. *Polymer* **1999**, *40* (23), 6361−6368.
(35) Li, Y.; Yuan, S.; Zhou, C.; Zhao, Y.; Van der Bruggen, B. A High Flux Organic Solvent Nanofiltration Membrane from Kevlar Aramid Nanofibers with *in Situ* Incorporation of Microspheres. *J. Mater. Chem. A* **2018**, *6* (45), 22987−22997.
(36) Gu, S.; Li, L.; Liu, F.; Li, J. Biochar/Kevlar Nanofiber Mixed Matrix Nanofiltration Membranes with Enhanced Dye/Salt Separation Performance. *Membranes* **2021**, *11* (6), 443.
(37) Cadotte, J. E.; Rozelle, L. T. *In-Situ-Formed Condensation Polymers for Reverse Osmosis Membranes*; PB229337; North Star Research and Development Inst.: Minneapolis, MN, 1972.
(38) Venyaminov, S. Yu.; Kalnin, N. N. Quantitative IR Spectrophotometry of Peptide Compounds in Water (H_2O) Solutions. II. Amide Absorption Bands of Polypeptides and Fibrous Proteins in α-, β-, and Random Coil Conformations. *Biopolymers* **1990**, *30* (13−14), 1259−1271.
(39) Larkin, P. *Infrared and Raman Spectroscopy: Principles and Spectral Interpretation*; Elsevier: Saint Louis, MO, 2011.
(40) Englander, S. W.; Sosnick, T. R.; Englander, J. J.; Mayne, L. Mechanisms and Uses of Hydrogen Exchange. *Curr. Opin. Struct. Biol.* **1996**, *6* (1), 18−23.
(41) Brackman, J. C.; Engberts, J. B. F. N. Effect of Water-Soluble Polymers on Rodlike and Spherical Micelles Formed from 2-Alkylmalonate Salts. *Langmuir* **1991**, *7* (1), 46−50.
(42) Sato, T.; Hamada, M.; Teramoto, A. Solution Viscosity of a Moderately Stiff Polymer: Cellulose Tris(Phenyl Carbamate). *Macromolecules* **2003**, *36* (18), 6840−6843.
(43) Fox, T. G.; Flory, P. J. Viscosity-Molecular Weight and Viscosity-Temperature Relationships for Polystyrene and Polyisobutylene. *J. Am. Chem. Soc.* **1948**, *70* (17), 2384−2395.
(44) Mouhamad, Y.; Mokarian-Tabari, P.; Clarke, N.; Jones, R. A. L.; Geoghegan, M. Dynamics of Polymer Film Formation during Spin Coating. *J. Appl. Phys.* **2014**, *116* (12), 123513.
(45) Baig, M. I.; Pejman, M.; Willott, J. D.; Tiraferri, A.; de Vos, W. M. Polyelectrolyte Complex Hollow Fiber Membranes Prepared via Aqueous Phase Separation. *ACS Appl. Polym. Mater.* **2022**, *4* (2), 1010−1020.
(46) Blanco, J.-F.; Sublet, J.; Nguyen, Q. T.; Schaetzel, P. Formation and Morphology Studies of Different Polysulfones-Based Membranes Made by Wet Phase Inversion Process. *J. Membr. Sci.* **2006**, *283* (1), 27−37.
(47) Dow-Filmtec-NF270−400.Pdf.
(48) Liptak, M. D.; Gross, K. C.; Seybold, P. G.; Feldgus, S.; Shields, G. C. Absolute PKa Determinations for Substituted Phenols. *J. Am. Chem. Soc.* **2002**, *124* (22), 6421−6427.
(49) Geise, G. M.; Park, H. B.; Sagle, A. C.; Freeman, B. D.; McGrath, J. E. Water Permeability and Water/Salt Selectivity Tradeoff in Polymers for Desalination. *J. Membr. Sci.* **2011**, *369* (1), 130−138.
(50) Yan, H.; Miao, X.; Xu, J.; Pan, G.; Zhang, Y.; Shi, Y.; Guo, M.; Liu, Y. The Porous Structure of the Fully-Aromatic Polyamide Film in Reverse Osmosis Membranes. *J. Membr. Sci.* **2015**, *475*, 504−510.
(51) Song, X.; Smith, J. W.; Kim, J.; Zaluzec, N. J.; Chen, W.; An, H.; Dennison, J. M.; Cahill, D. G.; Kulzick, M. A.; Chen, Q. Unraveling the Morphology−Function Relationships of Polyamide Membranes Using Quantitative Electron Tomography. *ACS Appl. Mater. Interfaces* **2019**, *11* (8), 8517−8526.
(52) Fox, R. J.; Yu, D.; Hegde, M.; Kumbhar, A. S.; Madsen, L. A.; Dingemans, T. J. Nanofibrillar Ionic Polymer Composites Enable High-Modulus Ion-Conducting Membranes. *ACS Appl. Mater. Interfaces* **2019**, *11* (43), 40551−40563.
(53) Gao, J.; Wang, Y.; Norder, B.; Garcia, S. J.; Picken, S. J.; Madsen, L. A.; Dingemans, T. J. Water and Sodium Transport and Liquid Crystalline Alignment in a Sulfonated Aramid Membrane. *J. Membr. Sci.* **2015**, *489*, 194−203.
(54) Every, H. A.; Mendes, E.; Picken, S. J. Ordered Structures in Proton Conducting Membranes from Supramolecular Liquid Crystal Polymers. *J. Phys. Chem. B* **2006**, *110* (47), 23729−23735.
(55) Viale, S.; Jager, W. F.; Picken, S. J. Synthesis and Characterization of a Water-Soluble Rigid-Rod Polymer. *Polymer* **2003**, *44* (26), 7843−7850.
(56) Hegde, M.; Yang, L.; Vita, F.; Fox, R. J.; van de Watering, R.; Norder, B.; Lafont, U.; Francescangeli, O.; Madsen, L. A.; Picken, S. J.; Samulski, E. T.; Dingemans, T. J. Strong Graphene Oxide Nanocomposites from Aqueous Hybrid Liquid Crystals. *Nat. Commun.* **2020**, DOI: 10.1038/s41467-020-14618-0.
(57) Zlopasa, J.; Norder, B.; Koenders, E. A. B.; Picken, S. J. Origin of Highly Ordered Sodium Alginate/Montmorillonite Bionanocomposites. *Macromolecules* **2015**, *48* (4), 1204−1209.
(58) Haraguchi, K.; Kajiyama, T.; Takayanagi, M. Uniplanar Orientation of Poly(p-Phenylene Terephthalamide) Crystal in Thin Film and Its Effect on Mechanical Properties. *J. Appl. Polym. Sci.* **1979**, *23* (3), 903−914.

(59) Law, K.-Y. Definitions for Hydrophilicity, Hydrophobicity, and Superhydrophobicity: Getting the Basics Right. *J. Phys. Chem. Lett.* **2014**, *5* (4), 686−688.
(60) Baek, Y.; Kang, J.; Theato, P.; Yoon, J. Measuring Hydrophilicity of RO Membranes by Contact Angles via Sessile Drop and Captive Bubble Method: A Comparative Study. *Desalination* **2012**, *303*, 23−28.
(61) Akin, O.; Temelli, F. Probing the Hydrophobicity of Commercial Reverse Osmosis Membranes Produced by Interfacial Polymerization Using Contact Angle, XPS, FTIR. *FE-SEM and AFM. Desalination* **2011**, *278* (1), 387−396.
(62) Schäfer, A. I.; Nghiem, L. D.; Waite, T. D. Removal of the Natural Hormone Estrone from Aqueous Solutions Using Nanofiltration and Reverse Osmosis. *Environ. Sci. Technol.* **2003**, *37* (1), 182−188.
(63) Vrijenhoek, E. M.; Hong, S.; Elimelech, M. Influence of Membrane Surface Properties on Initial Rate of Colloidal Fouling of Reverse Osmosis and Nanofiltration Membranes. *J. Membr. Sci.* **2001**, *188* (1), 115−128.
(64) Coronell, O.; Mi, B.; Mariñas, B. J.; Cahill, D. G. Modeling the Effect of Charge Density in the Active Layers of Reverse Osmosis and Nanofiltration Membranes on the Rejection of Arsenic(III) and Potassium Iodide. *Environ. Sci. Technol.* **2013**, *47* (1), 420−428.
(65) Mänttäri, M.; Pihlajamäki, A.; Nyström, M. Effect of PH on Hydrophilicity and Charge and Their Effect on the Filtration Efficiency of NF Membranes at Different PH. *J. Membr. Sci.* **2006**, *280* (1), 311−320.
(66) Lee, H.; Venable, R. M.; MacKerell, A. D.; Pastor, R. W. Molecular Dynamics Studies of Polyethylene Oxide and Polyethylene Glycol: Hydrodynamic Radius and Shape Anisotropy. *Biophys. J.* **2008**, *95* (4), 1590−1599.
(67) Paul, M.; Jons, S. D. Chemistry and Fabrication of Polymeric Nanofiltration Membranes: A Review. *Polymer* **2016**, *103*, 417−456.
(68) López-Muñoz, M. J.; Sotto, A.; Arsuaga, J. M.; Van der Bruggen, B. Influence of Membrane, Solute and Solution Properties on the Retention of Phenolic Compounds in Aqueous Solution by Nanofiltration Membranes. *Sep. Purif. Technol.* **2009**, *66* (1), 194−201.
(69) On Experimental Parameters Characterizing the Reverse Osmosis and Nanofiltration Membranes' Active Layer. *J. Membr. Sci.* **2006**, *282* (1−2), 109−114.
(70) Coronell, O.; Mariñas, B. J.; Zhang, X.; Cahill, D. G. Quantification of Functional Groups and Modeling of Their Ionization Behavior in the Active Layer of FT30 Reverse Osmosis Membrane. *Environ. Sci. Technol.* **2008**, *42* (14), 5260−5266.

https://doi.org/10.1021/acsami.2c09810
ACS Appl. Mater. Interfaces 2022, 14, 36143−36156